

Physicochemical Characterization and Electrocatalytic Evaluation of Dendritic Core-shell Au@Pd/C Electrocatalysts for the Oxygen Reduction Reaction

E. Y. Cervantes-Aspeitia^{1,2}, M. L. Hernández-Pichardo^{1,*}, R. G. González-Huerta², P. Del Angel^{3,*}, M. Tufiño-Velázquez⁴

¹ Instituto Politécnico Nacional-ESIQIE, Laboratorio de Nanomateriales Sustentables, UPALM, México City, 07738, México.

² Instituto Politécnico Nacional-ESIQIE, Laboratorio de Electroquímica, UPALM, México City, 07738, México.

³ Instituto Mexicano del Petróleo, Caracterización de Materiales Naturales y Sintéticos, México City, 07730, México.

⁴ Instituto Politécnico Nacional-ESFM, Laboratorio de Física Avanzada, UPALM, México City, 07738, México.

*E-mail: pangel@imp.mx, mhernandezp@ipn.mx

Received: 6 June 2020 / Accepted: 21 July 2020 / Published: 10 August 2020

Dendritic core-shell Au@Pd nanoparticles supported on carbon (D-Au@Pd/C) were synthesized by the seed-growth method. Pd dendrite formation on the Au surface was attributed to the nucleation and epitaxial growth of Pd atoms on specific facets of the Au NPs in the presence of adsorbed CTAC. In contrast, anisotropic palladium growth occurred over the uncapped planes of the gold core. The composition, morphology, and particle size of these catalysts were analyzed by HRTEM, HAADF-STEM, EDS mapping, XRD, and XPS. The electrocatalytic performance of the as-prepared catalyst in the ORR was compared to that of a commercial Pd/C catalyst. The superior performance of the D-Au@Pd/C material was related to the porous Pd shell and the synergetic effects between both metals. The dendritic structure allowed for an increased number of exposed active sites, and the interplay between both metals favored the suppression of the adsorption of hydroxyl and super hydroxyl groups on the active sites, enhancing the ORR kinetics of the Pd shell in acidic media.

Keywords: Dendritic shape; Au@Pd Nanoparticles; Carbon, HAADF-STEM; Oxygen Reduction Reaction; Electrocatalysis.

1. INTRODUCTION

One of the most promising technologies to meet global energy demands is proton exchange

membrane fuel cells (PEMFCs) due to their high efficiency, low working temperatures, and low emissions [1]. This technology has provided the most promising devices to achieve commercialization of fuel cells. A key challenge in the development of more efficient PEMFCs is the sluggish reaction rate at the cathode, where the oxygen reduction reaction (ORR) is six orders of magnitude slower than at the anode [2]. Therefore, the development of innovative metallic materials to catalyze the cathodic reaction is a crucial factor for the commercialization of fuel cell systems [3]. Platinum is the most effective electrocatalyst for the ORR, but due to its scarcity, the recent advances in electrocatalysts for ORR have mainly focused on low- and nonplatinum materials, including platinum alloys, core-shell structures, and palladium-based catalysts with novel structures and compositions [4,5].

Pd-based materials are among the best candidates for ORR catalysis in acidic media. It has also been found that multimetallic Pd-based nanoparticles present several advantages for the ORR in comparison to the corresponding monometallic components [6,7]. The incorporation of a second metal, as well as the nanoparticle (NP) shape, also plays an important role in improving the catalytic effects of Pd for this reaction [8,9]. Thus, binary metallic core-shell nanoparticles have attracted attention due to their improved electrocatalytic properties, which can be tuned by controlling their size, shape, and interfacial structure [10–12]. The incorporation of a second metal (Pt, Ni, Co, Fe, Cu, Au) to form alloys [13,14] or core-shell structures [15,16] to enhance the Pd activity has also been studied.

In the case of bimetallic Au-Pd-containing systems, it has been reported that gold may increase the chemical stability of palladium and modify its electrochemical properties [17,18]. Recently, dendritic Au@Pd NPs have also attracted considerable attention due to their relatively high surface area and surface defects that result in increased electrocatalytic activity [19,20]. However, the electrochemical performance of dendritic Au@Pd NPs deposited on carbon has been scarcely reported. Additionally, to our knowledge, the effect of this type of architecture on the ORR has not been studied before. Therefore, the main objective of this work was to synthesize dendritic Au@Pd NPs supported on carbon and to investigate the influence of the dendritic structure on the oxygen reduction reaction.

2. EXPERIMENTAL

2.1. Reagents and Chemicals

Palladium chloride (PdCl_2), tetrachloroauric (III) acid ($\text{HAuCl}_4 \cdot \text{H}_2\text{O}$), cetyltrimethylammonium bromide (CTAB), cetyltrimethylammonium chloride (CTAC), sodium borohydride (NaBH_4), trisodium citrate (Na_3Cit), ascorbic acid (AA), and Nafion® (5%) were purchased from Sigma-Aldrich, and HCl was purchased from Fermont.

A 0.01 M solution of dihydrogen tetrachloropalladate (II) (H_2PdCl_4) was prepared by mixing 44.5 mg of PdCl_2 in 25 mL of an aqueous HCl (20 mM) solution under stirring at room temperature until complete dissolution. A commercial Pd/C catalyst (10% Pd mass loading) and Vulcan carbon XC-72R were obtained from PK Catalyst. The bimetallic sample was prepared with nominal contents of 5 wt. % Au and 5 wt. % Pd.

2.2. Synthesis of the dendritic Au@Pd/C catalysts by the seed-growth method

A three-step synthesis method was followed for the synthesis of the D-Au@Pd catalyst. The first step consists of the preparation of a seed solution similar to that reported by Jana and coworkers [22] to obtain Au nanoparticles 5 ± 0.8 nm in diameter. In a conical flask, 300 μL of HAuCl_4 (10 mM) and 2 mL of trisodium citrate (2.5 mM) were mixed. Next, 0.6 mL of ice-cold, freshly prepared NaBH_4 (0.1 M) solution was added to the mixture while stirring. The solution was kept under slow stirring for 3 h to assure the total decomposition of NaBH_4 . The second step was the preparation of the growth solution (octahedral Au nanoparticles). Two hundred microliters of HAuCl_4 (10 mM), 5 mL of CTAB (0.1 M), and 2 mL of ascorbic acid (0.1 M) were diluted in 35 mL of Milli-Q water. Then, 0.3 mL of seed solution was added, mixed for 3 min, and left undisturbed overnight. In the third step, a dendritic core-shell Au@Pd nanoparticle solution was prepared. Four milliliters of the growth solution was mixed with 32 mL of Milli-Q water, and 5 mL of CTAC (0.1 M) was mixed with 400 μL of H_2PdCl_4 (0.01 M). These solutions were mixed and stirred for 3 min; after this, 0.1 mL of ascorbic acid (0.1 M) was added. The solution was mixed for 10 min and left undisturbed overnight. Finally, the supported D-Au@Pd/C NPs were prepared by mixing Vulcan carbon, ethanol, and the D-Au@Pd NP solution together and drying at 90 °C for 8 h to obtain a load of 5 wt. % Au and 5 wt. % Pd.

2.3. Electrochemical measurements

Electrocatalytic inks were prepared by mixing 5 mg of catalyst powder with 750 μL of isopropanol, 250 μL of Milli-Q water, and 70 μL of Nafion® solution. The mixture was sonicated for 45 min, and then, 9 μL of this suspension was dropped on a glassy carbon electrode (0.196 cm^2) previously polished to a mirror finish. The Pd loading on the glassy carbon was 21.5 $\mu\text{g cm}^{-2}$ and 10.7 $\mu\text{g cm}^{-2}$ in the commercial Pd/C and D-Au@Pd/C electrodes, respectively, which is consistent with the literature recommendation [23]. Finally, the glassy carbon electrode was dried by rotating at 500 rpm at room temperature. All electrochemical experiments were carried out using an Autolab PGSTAT302N potentiostat. For all the electrochemical measurements, a standard three-electrode glass cell was used. A Pt mesh and a reversible hydrogen electrode (RHE) were used as counter and reference electrodes, respectively. A glassy carbon rotating disk electrode (RDE) was used as a working electrode, and the electrolyte was 0.1 M HClO_4 . The electrochemical measurements were carried out at 25 °C. Cyclic voltammetry (CV) and linear sweep voltammetry (LSV) techniques were carried out in saturated Ar and O_2 , respectively. The CV profiles were recorded from 0.05 to 1.2 V vs. RHE at 50 mV s^{-1} . LSV polarization curves were obtained from the open circuit potential (OCP) to 0.25 V vs. RHE at 5 mV s^{-1} , with rotation speeds of 100, 200, 400, 900 and 1600 rpm. The electrocatalytic activity in the oxygen reduction reaction (ORR) was evaluated in 0.1 M HClO_4 . The CO-stripping technique was used to calculate the electrochemical active surface area (ECSA). First, the solution was saturated with CO for 5 min, and, finally, the residual CO in the solution was removed by bubbling with Ar for 20 min, all under a set potential of 0.1 V vs. RHE.

2.4. Structural characterization

XRD patterns were collected on a Bruker AXS D8 diffractometer with Cu K α radiation ($\lambda = 1.5418 \text{ \AA}$). High-resolution transmission electron microscopy (HRTEM) images were acquired on an FEI TITAN 80-300 operated at 300 kV with a Cs corrector. Scanning transmission electron microscopy (STEM) analyses were conducted on a JEOL JEM-ARM 200CF operated at 200 kV and equipped with a Cs probe corrector. In this instrument, high-angle annular dark field (HAADF-STEM) images, chemical compositions, mapping, and line scanning profiles were obtained by energy dispersive spectroscopy (EDS-STEM). Samples for HRTEM and STEM analyses were prepared by depositing a single drop of a diluted NP dispersion in isopropanol on lacey formvar/carbon-coated copper grids. X-ray photoelectron spectroscopy (XPS) was carried out using a K-alpha spectrometer with a monochromatic Al ka X-ray source (1486.6 eV) from Thermo Fischer Scientific.

3. RESULTS AND DISCUSSION

3.1. High-resolution transmission electron microscopy (HRTEM) and scanning transmission electron microscopy (STEM)

HRTEM images at the atomic level were obtained to explore the growth mechanism and Pd aggregation state over the Au nanoparticles. The analyses were carried out for the materials at all three synthesis steps: monometallic Au seeds, octahedral Au NPs, and bimetallic D-Au@Pd/C. Figure 1(a) presents a TEM image of the Au seeds, showing the formation of spherical Au NPs with an average size of $5 \pm 0.8 \text{ nm}$. In this case, trisodium citrate was used as a reducing and stabilizing agent of the size; the citrate ions changed the negative surface charge, causing the nanoparticles to repel from each other, thus preventing the growth of the Au seeds. In addition, sodium borohydride has a high capacity for reduction, producing a large number of Au seeds. Due to its high nucleation ability, it did not allow the growth of the particles, generating a high concentration of Au NPs [24]. Figure 1(b) shows the HRTEM image of one Au seed, with a zone axis of [02-2]. Figure 1(c) shows the HRTEM image of an octahedral Au nanoparticle from the growth solution, having an average size of $25 \pm 1.6 \text{ nm}$. Since ascorbic acid is not a strong reducing agent, it allowed the heterogeneous deposition of gold on the surface of the seeds, and, along with the use of CTAB as a surfactant, it enabled the anisotropic growth of truncated NPs in an aqueous solution and prevented their aggregation [25]. The formation of typical twins of gold nanoparticles was observed; these defects allowed for the development of dendrites of the Pd over the Au nanoparticles. The FFT (inset) of the HRTEM image of this octahedral Au nanoparticle (Figure 1(d)) shows several spots. These spots are the contributions of the different faces (orientations) of the Au nanoparticle. Inside, it is possible to identify the [02-2] zone axis coming from one face of this nanoparticle.

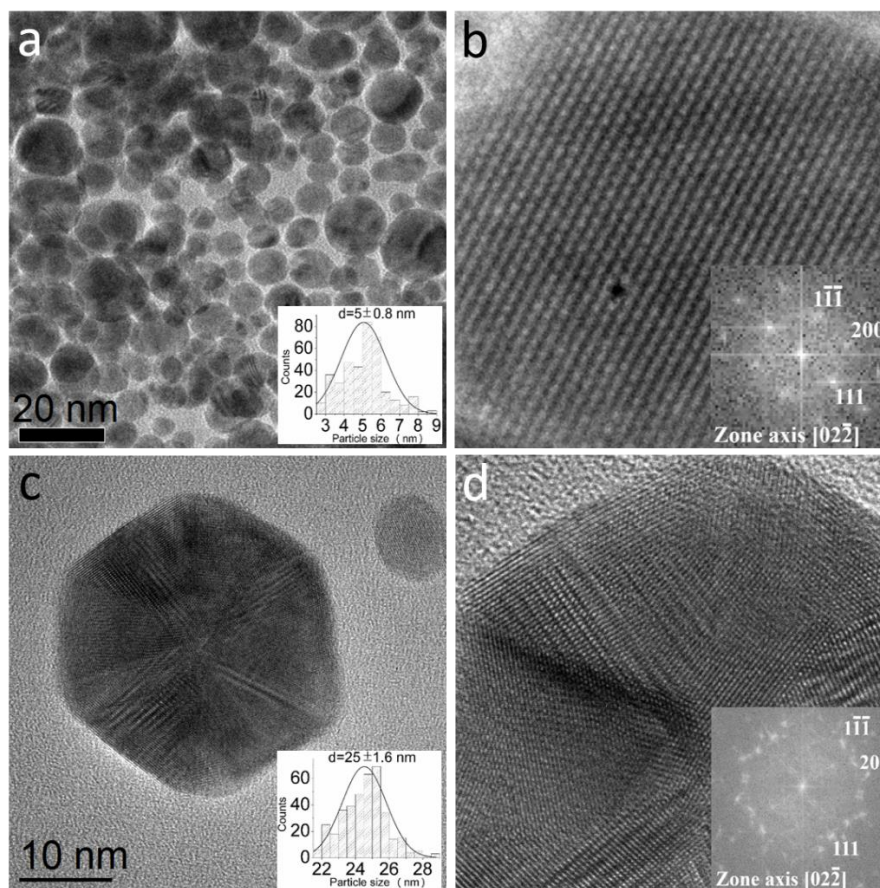


Figure 1. (a) TEM image of the Au seeds, with an average size of 5 nm, (b) HRTEM image of an Au seed with the [02-2] zone axis, (c) TEM image of octahedral Au nanoparticles with an average size of 25 nm and (d) HRTEM of the same Au nanoparticle showing characteristic twins and Moirés. The FFT (inset) shows different spots; some of them correspond to the [02-2] zone axis.

The morphology of the D-Au@Pd NPs with an average size of 35 ± 2.5 nm is shown at intermediate magnification in Figure 2(a). According to the mass-thickness contrast effect, the Au-rich center of the nanoparticle presents a dark contrast compared with their Pd-rich edges. Some studies have reported that the rapid growth of metals in a CTAC solution contributed to the fast formation of metallic shells on gold nanostructures, generating a nonuniform growth of the shell over the Au core [26]. Higher magnification images of dendritic Au@Pd NPs are shown in Figure 2(b). Irregular growth of Pd over Au was observed. Figure 2(c) shows an HRTEM image of the Au@Pd NP edge, where the interplanar distances were measured by using FFT exhibiting a palladium fcc structure with a zone axis of [02-2]. It was not possible to measure the Au planes because the region with gold was too thick. Figure 2(d) shows the EDS spectrum, and semiquantitative analysis of the nanoparticle shows a composition of 39% for Au and 61% for Pd. This result is not consistent with the theoretical stoichiometric proportion of 1:1 because of the overlapping signal effect due to the Pd thickness, which caused the Au signal to decrease. The Cu peak corresponds to the copper grid. Fe peaks correspond to iron in the grid holder.

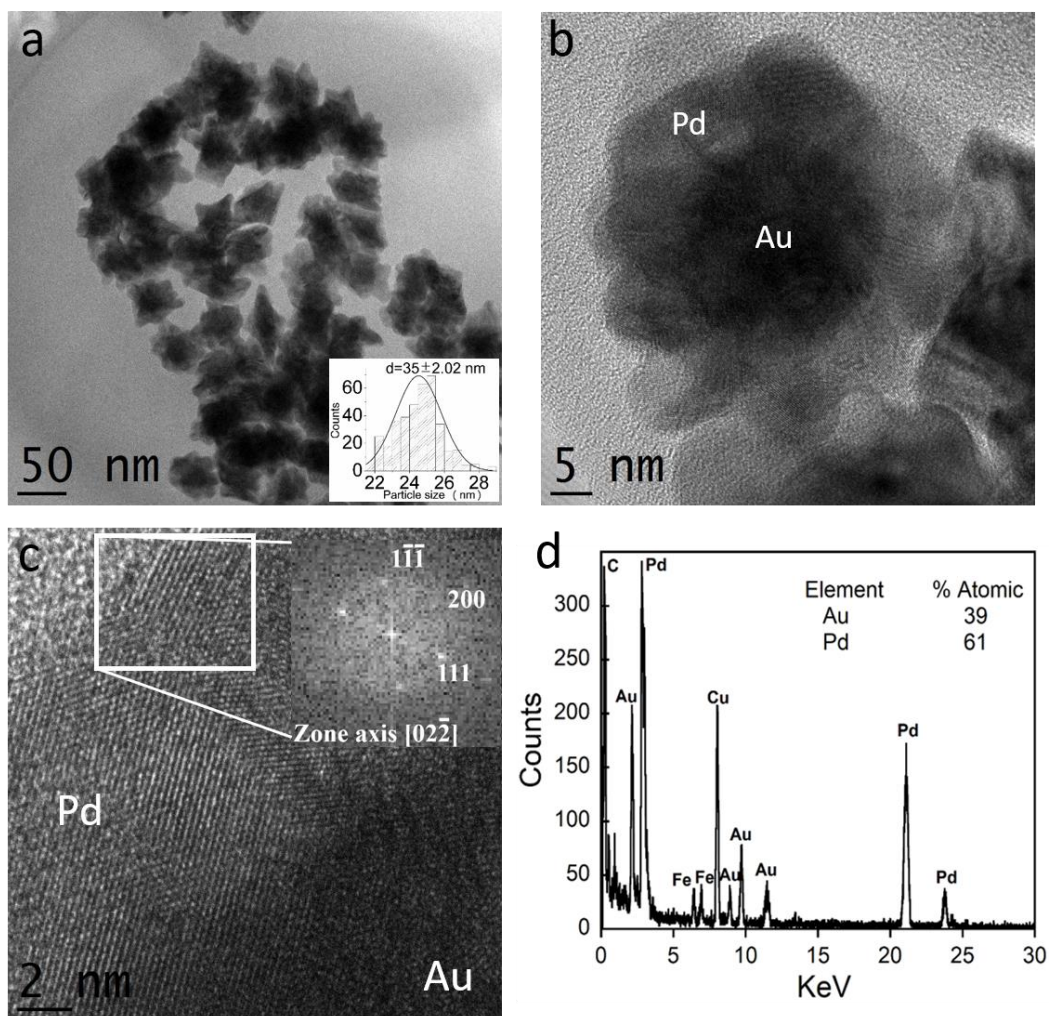


Figure 2. (a) Morphology of dendritic-like Au@Pd core-shell NPs with an average size of 35 nm, (b) irregular growth and different densities of dendritic Au@Pd NPs, (c) HRTEM image of dendritic Au@Pd NPs and (d) EDX spectrum and semiquantitative analysis of Au@Pd core-shell nanoparticles.

To confirm the formation of the dendritic Au@Pd structure at the atomic level, a deeper analysis by using HAADF-STEM, EDS elemental mapping, and EDS line scanning profiles was performed. The HAADF-STEM image at low magnification in Figure 3(a) shows the dendritic Au@Pd core-shell NPs supported on Vulcan carbon. Figure 3(b) shows an Au@Pd nanoparticle obtained at intermediate magnification; this nanoparticle exhibits a contrast between the Au core (atomic number 79) and the Pd shell (atomic number 46). Considering that the HAADF-STEM technique can distinguish chemical elements with an atomic number difference ≥ 7 , this was the case for Au, which is heavier than Pd. In the same D-Au@Pd nanoparticle, high-resolution HAADF-STEM images from two different regions were obtained for Pd (Figure 3(c)) and Au (Figure 3(d)), indicated by red and green squares, respectively. Over the red square, the measured interplanar distance was 0.224 nm, corresponding to the (111) plane of the metallic palladium with an fcc structure. The measurement in the green square was 0.236 nm, which corresponds to the (111) plane of metallic gold, with the same fcc structure as that of Pd. The atomic plane measurements confirmed that palladium covered the gold NP surface. Since Au and Pd

have the same crystallographic structure (fcc), they present a high lattice match, and it was possible to observe the continuation of the atomic planes from the core (Au) to the shell (Pd) along the (111) plane. This result confirms the epitaxial growth of Pd on some Au facets.

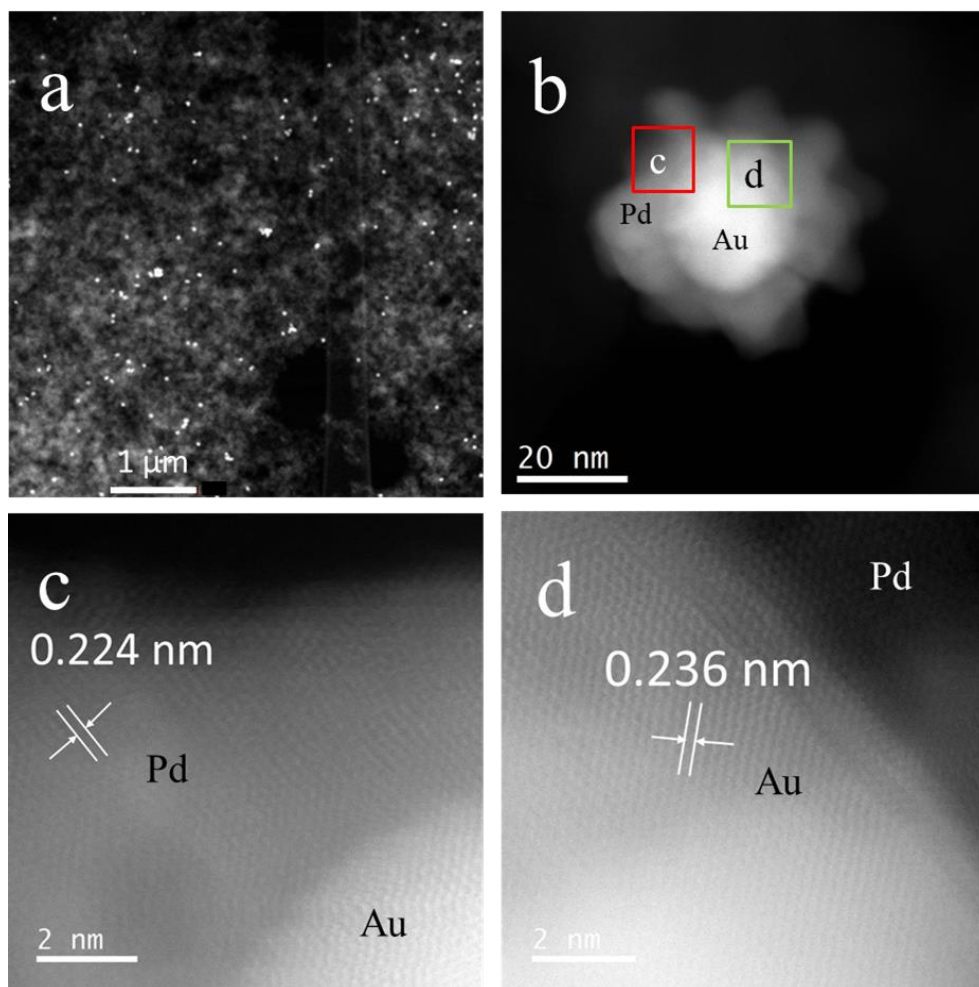


Figure 3. (a) HAADF image of the D-Au@Pd supported on Vulcan carbon, (b) HAADF of D-Au@Pd NP showing the Au core and the Pd shell in regions c and d, respectively, (c) high-resolution HAADF image of the Pd shell and (d) high-resolution HAADF image of the Au core.

The corresponding EDS line scanning profile is shown in Figure 4(a). This corroborates that the D-Au@Pd NPs consist of an Au-rich center (green line) and a Pd-rich edge (red line). The EDS elemental mapping of the same particle is shown in Figures 4(b)-(c). The elemental mapping (Figure 4(d)) indicates that Pd is entirely covering the gold particle because its signal is continuous over all the nanoparticles. The Au core maintains a size of approximately 25 nm, and the Pd shell thickness is approximately 12-15 nm.

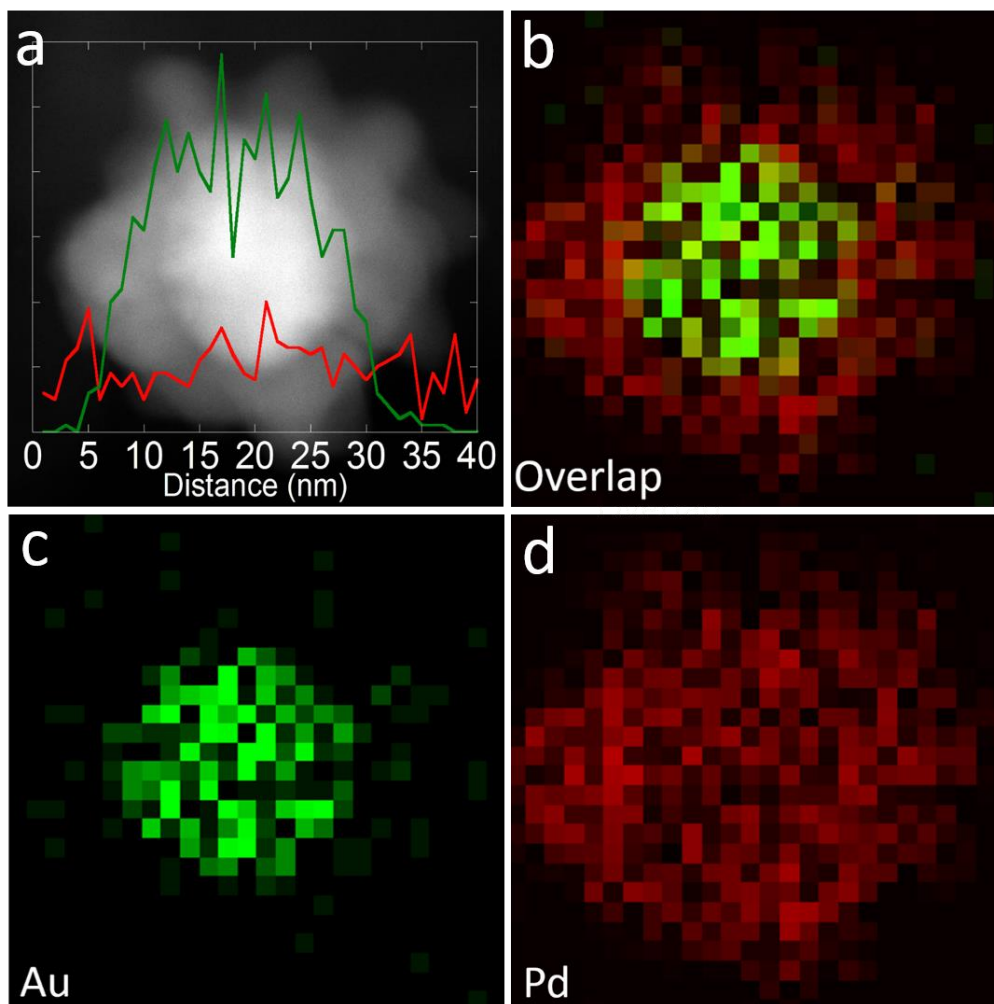


Figure 4. (a) EDS line scanning profiles of a D-Au@Pd nanoparticle (Au is in green and Pd is in red), (b)-(d) its corresponding EDS elemental mapping.

In the seed-mediated growth method, both thermodynamic and kinetic factors should be taken into consideration for understanding the formation mechanism of Pd dendrites [27]. If kinetic factors prevail, the shape of Pd nanocrystals will be determined by the growth rate of different crystal faces. In this sense, the chemical species used (reducing, stabilizing, or capping agents) for the preparation of core-shell nanoparticles may also play a key role in the overgrowth process since they may modify the growth kinetics [6,28]. In this work, it was observed that the growth mechanism of Pd over the Au surface using this synthesis method led to the formation of a dendritic-type porous Pd shell covering the Au core. This fact was attributed to the poor CTAC capping ability because this surfactant exhibits weaker electrostatic interactions than those of CTAB. It has been reported that the binding strength of halides to the Au particle surface increases in the order of $\text{Cl}^- < \text{Br}^- < \text{I}^-$ [29]. Moreover, theoretical studies have found that Cl^- ions preferentially remain in solution, in contrast to Br^- ions, which are strongly adsorbed onto the gold surface [30].

Thus, by using CTAC in the synthesis for Pd growth, some crystal Au planes remain uncapped and exposed to Pd nucleation. Thus, the slow reduction by using AA favored Pd growth on those facets. The formation of some dendrites was ascribed to the nucleation and epitaxial growth of Pd atoms over

some facets of the Au NPs. This nonuniform growth occurred because CTAC was partially adsorbed on the gold surface since Cl^- ions preferentially remain in the solution [30]. In contrast, anisotropic growth occurred on the uncapped planes of the gold core, forming a heterogeneous shell.

3.2. X-ray diffraction (XRD) and X-ray photoelectron spectroscopy (XPS)

XRD patterns for D-Au@Pd/C and the commercial Pd/C samples are shown in Figure 5. The reflection peaks at 40.1° , 46.5° and 68° in 2-theta correspond to the (111), (200) and (220) atomic planes of the metallic Pd (01-089-4897 JCPDS card), respectively. The (111) peak of Pd is observed in both samples. The other two characteristic reflections for Pd at (200) and (220) are not clearly observed due to the polycrystalline nature (high background) of the Vulcan carbon support (00-050-0926 JCPDS card). The Au peaks (00-001-1172 JCPDS card) are at 38.2° , 44.5° , and 64.89° in 2-theta; however, in the Au@Pd/C sample, only the (111) reflection is observed due to the high Vulcan carbon background. The peak positions of the core-shell nanoparticles correspond to pure Au and Pd metals with an fcc structure, according to the JCPDS cards, confirming that the Pd shell is thick enough to produce reflections assigned to Pd^0 . The PdO in the commercial sample is observed to be a small, broad peak at 33.5° in 2-theta corresponding to the (022) plane of PdO (43-1024 JCPDS card).

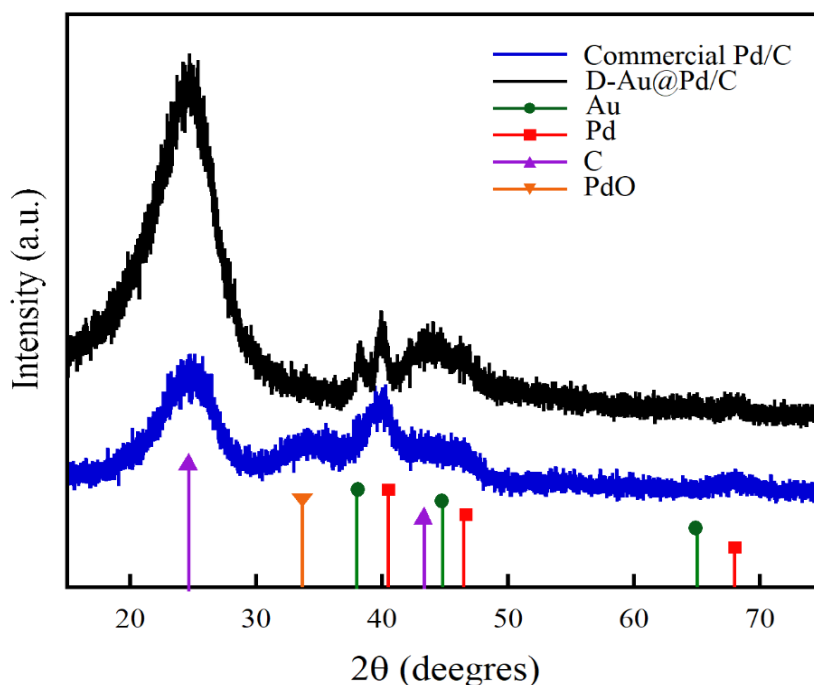


Figure 5. XRD patterns of D-Au@Pd/C and commercial Pd/C samples.

The XPS results are shown in Figure 6. Figure 6(a) presents the general XPS spectra for the D-Au@Pd/C catalyst, verifying the presence of Au, Pd, and C in the as-prepared sample. The intensity of the Au signal is quite low compared to that of Pd. Considering the results obtained by HRTEM, these results indicate that the metal on the surface is mainly palladium since XPS analysis is a surface-sensitive technique. This result confirms those obtained by HAADF, which showed the formation of the Pd shell (thickness of approximately 12-15 nm) and corroborated the formation of core-shell Au@Pd NPs. The

Au 4f and Pd 3d high-resolution spectra for the D-Au@Pd/C sample are shown in Figure 6(b)-(d). For the D-Au@Pd/C sample, the binding energy of Au 4f was found at 87.4 eV and 83.5 eV, corresponding to $4f_{5/2}$ and $4f_{7/2}$, respectively, assigned to Au at the zero-valent state [31]. The XPS spectra of D-Au@Pd/C and commercial Pd/C for Pd 3d are shown in Figures 6(c)-(d), and they were deconvoluted into two pairs of doublets. For the D-Au@Pd/C catalyst, the most intense doublets at 335.2 and 340.5 eV correspond to metallic Pd. The weakest doublets (336.7 and 342.6 eV) were assigned to Pd in the oxidized state, showing that Pd is not completely reduced to metallic palladium [21]. According to the peak intensity, the surface atomic ratio of Pd to Au is approximately 9:1, indicating that Pd atoms mainly form the surface and that not all Au particles are covered by gold. Similarly, the spectrum of the commercial Pd/C catalyst can also be deconvoluted into two doublets related to Pd^0 (335.2 and 340.6 eV) and Pd^2+ (336.6 and 341.9 eV). Thus, compared to the Pd $3d_{5/2}$ and $3d_{3/2}$ binding energies of the D-Au@Pd/C catalyst, no apparent shift was observed in the Au@Pd/C catalyst, probably due to the large Pd shell thickness of the Au@Pd/C.

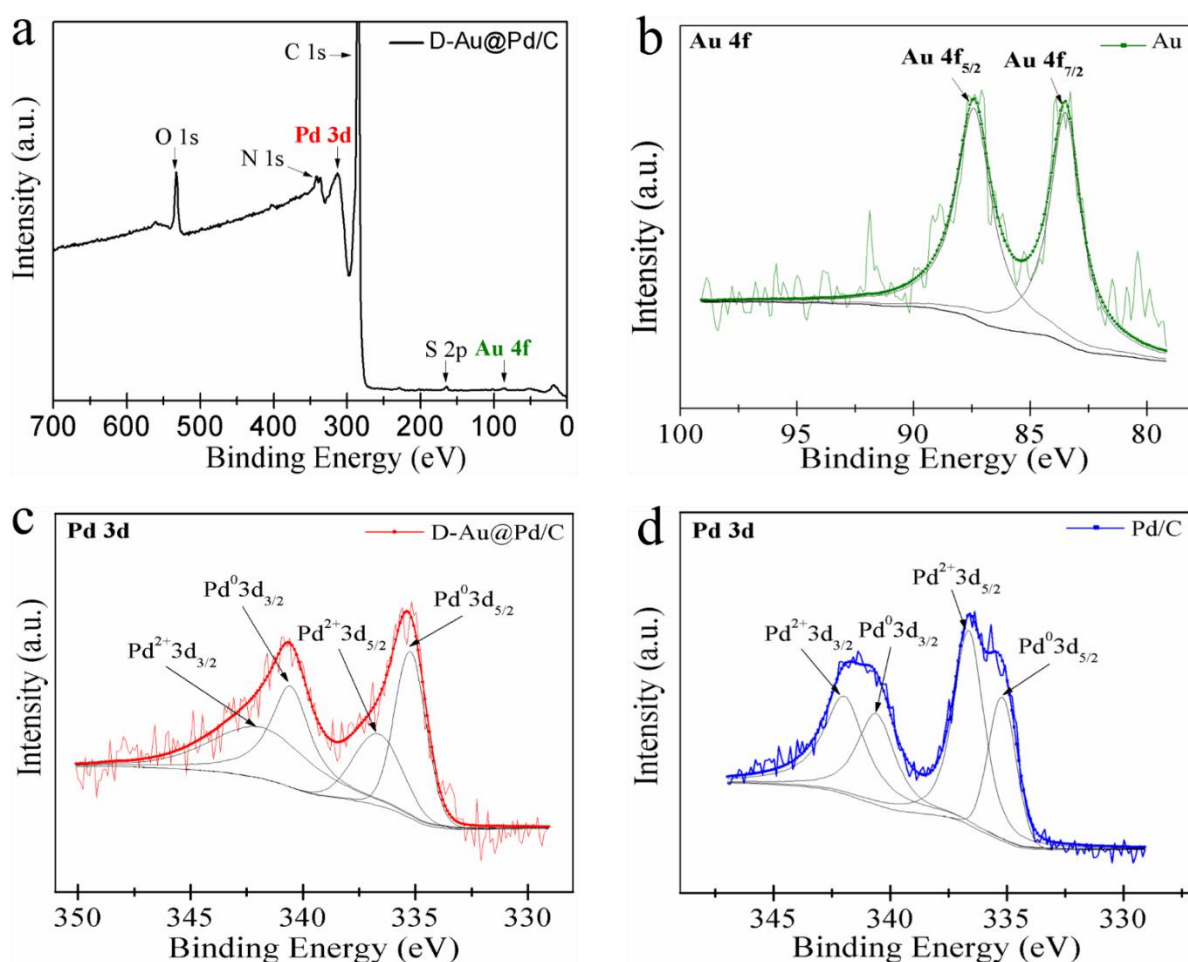


Figure 6. a) XPS general spectra for D-Au@Pd/C, b) high-resolution XPS spectra for Au 4f, c), and d) high-resolution XPS spectra for Pd 3d for D-Au@Pd/C and commercial Pd/C.

3.3. Electrochemical characterization

Electrochemical studies of the D-Au@Pd/C and commercial Pd/C catalysts were performed in

HClO₄. The current density was normalized to 1 mg of palladium loading and the geometrical area of the glassy carbon electrode. The cyclic voltammograms (CV) of D-Au@Pd/C and commercial Pd/C materials were evaluated in an Ar-saturated atmosphere with a scan rate of 50 mV s⁻¹. Figure 7(a) shows the electrochemical behavior in a potential window from 0.05 to 1.2 V/RHE, starting at an open circuit potential of 0.870 V/RHE and moving in the positive direction. Regions of hydrogen adsorption/desorption can be observed at the potential interval ranging from 0.05 to 0.38 V/RHE, where a higher current density for D-Au@Pd/C than for the commercial Pd/C electrode was obtained. The D-Au@Pd/C electrode did not present the characteristic voltammogram associated with the adsorption/desorption of hydrogen of polycrystalline noble metals. This could be due to a relatively large particle size [10] and irregular and porous Pd shell, which may favor hydrogen adsorption on different planes. The Pd-O onset potentials were 0.85 and 0.74 V/RHE for D-Au@Pd/C and the commercial Pd/C electrode, respectively. This shift of 0.09 V/RHE was attributed to the interaction between the Au core and Pd shell because the adsorption of hydroxyl and super hydroxyl groups on active sites was suppressed [32,33]. The reduction peak potential has a positive shift of 30 mV between the two materials, being 0.75 and 0.72 V/RHE for D-Au@Pd/C and the commercial Pd/C electrode, respectively. This result indicates that the oxides formed on D-Au@Pd/C are more easily reduced than the oxides formed on Pd/C, suggesting that the developed catalyst would be a better catalyst than the commercial Pd/C catalyst in the ORR.

The typical ORR linear sweep voltammetry plots for both samples are shown in Figure 7b, where the OCP values had a difference of 0.03 V/RHE, being higher for D-Au@Pd/C than for Pd/C and consistent with a positive shift of the reduction peak potential observed in the CV. The half-wave potentials ($E_{1/2}$) decreased in the order of 0.79 V/RHE (D-Au@Pd/C) > 0.76 V/RHE (commercial Pd/C), which presents a shift of 30 mV to more positive values, demonstrating an increase in the electrocatalytic activity toward the ORR. The enhanced electrochemical activity of D-Au@Pd/C compared to the commercial Pd/C electrode is related to the porous dendritic structure, which exhibits a larger specific area and a higher number of active sites, probably generated by a significant amount of defects on the surface [34,35]. The way Pd nanoparticles grew on the gold surface prevented agglomeration because they are independent of each other, making them more efficient. In addition, using Eq. (1) [36], the ECSA was calculated from the CO stripping reaction at the electrode interface in an acidic medium (0.1 M HClO₄).

$$ECSA_{CO} \text{ (m}^2\text{g}^{-1}\text{)} = \left[\frac{Q_{CO}(C)}{420 \text{ (}\mu\text{C cm}^{-2}\text{)}L_{Pd}(\text{mg cm}^{-2}\text{)}A_g(\text{cm}^2)} \right] 10^5 \quad (1)$$

where Q_{CO} is the charge of CO-induced adsorption, 420 ($\mu\text{C cm}^{-2}$) is the charge required to oxidize the monolayer of CO, L_{Pd} is the Pd catalyst loading on the working electrode, and A_g is the geometric surface area of the glassy carbon electrode (0.196 cm²). Figures 7c-d show the CO stripping voltammograms for D-Au@Pd/C and commercial Pd/C catalysts, where the peaks associated with CO oxidation to CO₂ were found at 1.04 V/RHE and 0.91 V/RHE for D-Au@Pd/C and the commercial Pd/C electrode, respectively. The electrochemical surface area, the obtained CO stripping reaction parameters, and the kinetic parameters for D-Au@Pd/C, commercial Pd/C and reported Au@Pd catalyst for oxygen reduction reaction are described in Table 1. According to the obtained results, ECSA for the D-Au@Pd/C catalyst is 1.17 times higher than one for the commercial Pd/C catalyst.

Table 1. Comparison of electrochemical values and kinetics parameters for D-Au@Pd/C, commercial Pd/C and reported Au@Pd catalyst for oxygen reduction reaction

Synthesis method	Morphology and size	Support	$E_{(1/2)}$ [V vs. RHE]	ECSA [$\text{m}^2 \text{g}^{-1}$]	$E_{\text{onset-CO}}$ [E/V vs. RHE]	I_{CO} [$\text{mA cm}^{-2} \text{mg}^{-1}$]	E_{CO} [E/V vs. RHE]	b [mV dec^{-1}]	α	Reference
Seed-mediated growth	Dendritic core-shell 35.5 nm	Vulcan carbon	0.79	86.3	0.91	859.6	1.04	61.45	0.988	This work data
Unknown for commercial Pd/C	Spherical 3.5 nm	Vulcan carbon	0.76	73.4	0.68	699.8	0.91	64.35	0.910	This work data
Via core-shell Au@Ag/Pd constructions	Spherical 12.5 nm	Vulcan carbon	0.74	64.7	0.91	105.6	0.98	--	--	[21]
Seed-mediated growth	Cuboctahedral 69.6 nm	Vulcan carbon	0.84	--	--	--	--	95.2	--	[8]
Co-chemical reduction	Nanorhorns 30-50 nm	No support	0.85	10.48	0.84	73.8	0.89	--	--	[9]

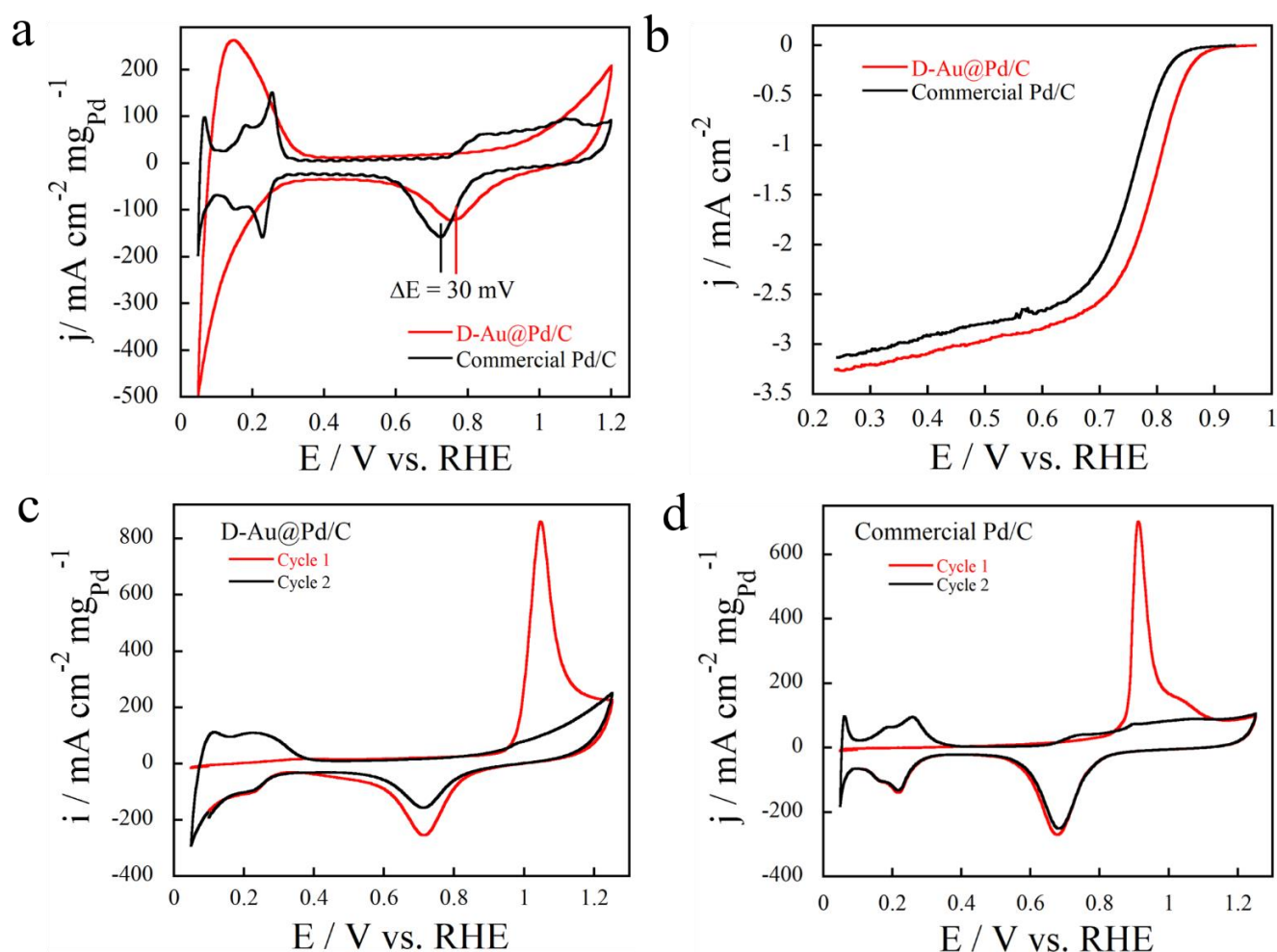
**Figure 7.** Electrochemical measurements in an HClO_4 solution. (a) CVs for D-Au@Pd/C and commercial Pd/C in Ar saturated atmosphere at a scan rate of 50 mV s^{-1} , (b) ORR polarization curves for D-Au@Pd/C and commercial Pd/C in O_2 saturated solution at a scan rate of 5 mV s^{-1} and a rotation rate of 1,600 rpm, (c) and (d) CO stripping voltammograms at a scan rate of 20 mV s^{-1} for D-Au@Pd/C and the commercial Pd/C electrode, respectively.

Figure 8(a) shows the polarization curves at different rotation rates of the D-Au@Pd/C catalyst in an oxygen-saturated atmosphere and a 0.1 M HClO₄ solution at 25 °C. The main characteristics in the polarization curve are the defined charge transfer control and the mixed and mass transfer region. The inset figure represents the Koutecky–Levich plot for the D-Au@Pd/C catalyst, where the inverse current density (j^{-1}) is a function of the inverse of the square root of the rotation rate ($\omega^{-1/2}$). The linearity of these lines indicates that the number of electrons transferred in the reaction does not change significantly within the studied potential range. Figure 8(b) shows the Tafel plot, where the slopes were determined a range at more positive potentials, and the measured current densities were mainly due to electronic transfer control for the ORR. In this region, kinetic parameters such as Tafel slope value (b) and transfer coefficient (α), which are reported in Table 1, were calculated respecting that this range covers a minimum of one decade of current. The potential values, E , which were obtained for $j=0.01$ mA cm⁻², in the order of 0.94 and 0.90 V vs. RHE for D-Au@Pd/C and commercial Pd/C, respectively.

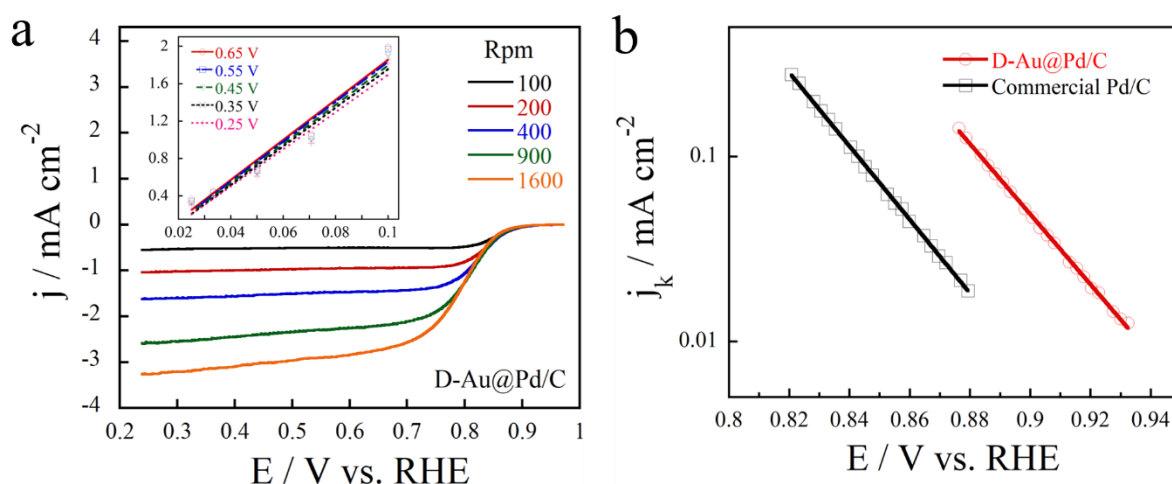


Figure 8. (a) ORR polarization curves for the D-Au@Pd/C catalyst at different rotation rates in an oxygen-saturated atmosphere and in a 0.1 M HClO₄ electrolyte. The inset shows the Koutecky-Levich plot at various electrode potentials and (b) Tafel slopes for the D-Au@Pd/C and commercial Pd/C catalysts.

In summary, the Tafel slope values of approximately 60 mV dec⁻¹ determined on these samples (D-Au@Pd/C and commercial Pd/C) at low overpotentials are in good agreement with those reported in the literature [37] and is explained in terms of an electrode surface saturated with adsorbed oxygen, where the rate-determining step of the overall molecular oxygen reduction is controlled by the first charge-transfer step, i.e., $(O_2)_{ads} + e^- \rightarrow (O_2^-)_{ads}$. The transfer coefficient values are consistent with the obtained Tafel slopes. However, the higher potential reached (0.94 V) at 0.01 mA cm⁻² for the D-Au@Pd/C catalyst with respect to the potential reached by the commercial Pd/C catalyst (only 0.90 V), should be noted. These results indicate that the D-Au@Pd/C catalyst exhibited enhanced catalytic activity toward the oxygen reduction reaction compared to that of the commercial Pd/C catalyst in a perchloric acid solution. The improved catalytic activity should be attributed to two principal reasons: (a) the way that the Pd grew on the Au surface allowed for the formation of a porous core-shell structure

and exposed a high number of active sites to adsorb oxygen. This provided an increase in the electrochemical surface area and the number of active sites, which is favorable for the enhancement of catalytic activity [35], and (b) the interaction between Au and Pd modified the electronic structure of Pd, resulting in the ability to suppress the adsorption of hydroxyl and super hydroxyl groups on active sites, thus providing a synergistic effect to increase the catalytic activity of Pd [32,38].

4. CONCLUSIONS

In the present work, a dendritic core-shell D-Au@Pd/C catalyst was successfully prepared by a seeded-growth method. HRTEM, HAADF-STEM and XPS results directly showed the epitaxial growth of Pd over Au facets, forming dendritic core-shell D-Au@Pd/C nanoparticles. The electrocatalytic activity of these NPs was compared to that of a commercial Pd/C catalyst. The slow Pd reduction in the presence of CTAC over the Au surface resulted in the formation of a porous shell, which increased the electrochemical surface area. The D-Au@Pd/C catalyst exhibited a higher oxygen reduction reaction activity than commercial Pd/C in acidic media due to the porous Pd surface, with a larger specific area, more exposed active sites, and the synergetic effects between the Au core and the Pd shell. The interaction between both metals suppressed the adsorption of hydroxyl and super hydroxyl groups on the active sites, thus enhancing the catalytic activity. The D-Au@Pd/C catalyst is a promising candidate for use as a cathode electrocatalyst in proton exchange membrane fuel cells.

ACKNOWLEDGMENTS

This work was supported by the Instituto Politécnico Nacional [20200541 and SIP-2024], CONACyT [CB A1-S15770] and CEMIE Océano [249795]. E.Y.C.A. thanks the financial support from CONACyT [Ph.D. scholarship number 787438].

References

1. Y. Wang, K.S. Chen, J. Mishler, S.C. Cho, X.C. Adroher, *Appl. Energy*, 88 (2011) 981–1007.
2. L. Zhang, S.R. Chae, Z. Hendren, J.S. Park, M.R. Wiesner, *Chem. Eng. J.*, 204–205 (2012) 87–97.
3. K. Vignarooban, J. Lin, A. Arvay, S. Kolli, I. Kruusenberg, K. Tammeveski, L. Munukutla, A.M. Kannan, *Chinese J. Catal.*, 36 (2015) 458–472.
4. Y. Wang, J. Li, Z. Wei, *ChemElectroChem*, 5 (2018) 1764–1774.
5. M. Shao, P. Liu, J. Zhang, R. Adzic, *J. Phys. Chem. B*, 111 (2007) 6772–6775.
6. Y.W. Lee, M. Kim, Z.H. Kim, S.W. Han, *J. Am. Chem. Soc.*, 131 (2009) 17036–17037.
7. L. Kuai, X. Yu, S. Wang, Y. Sang, B. Geng, *Langmuir*, 28 (2012) 7168–7173.
8. A. Romero Hernández, M.E. Manríquez, A. Ezeta Mejia, E.M. Arce Estrada, *Electrocatalysis*, 9 (2018) 752–761.
9. G. Fu, Z. Liu, Y. Chen, J. Lin, Y. Tang, T. Lu, *Nano Res.*, 7 (2014) 1205–1214.
10. J.J. Salvador-Pascual, S. Citalán-Cigarroa, O. Solorza-Feria, *J. Power Sources*, 172 (2007) 229–234.
11. H. Erikson, A. Sarapuu, K. Tammeveski, J. Solla-Gullón, J.M. Feliu, *Electrochem. Commun.*, 13 (2011) 734–737.
12. A. Londono-Calderon, D. Bahena, M.J. Yacaman, *Langmuir*, 32 (2016) 7572–7581.

13. M.H. Shao, T. Huang, P. Liu, J. Zhang, K. Sasaki, M.B. Vukmirovic, R.R. Adzic, *Langmuir*, 22 (2006) 10409–10415.
14. V. Raghuvier, A. Manthiram, A.J. Bard, *J. Phys. Chem. B*, 109 (2005) 22909–22912.
15. X. Zhao, S. Chen, Z. Fang, J. Ding, W. Sang, Y. Wang, J. Zhao, Z. Peng, J. Zeng, *J. Am. Chem. Soc.*, 137 (2015) 2804–2807.
16. D. Wang, H.L. Xin, Y. Yu, H. Wang, E. Rus, D.A. Muller, H.D. Abruña, *J. Am. Chem. Soc.*, 132 (2010) 17664–17666.
17. K.A. Kuttiyiel, K. Sasaki, D. Su, L. Wu, Y. Zhu, R.R. Adzic, *Nat. Commun.*, 5 (2014) 5185.
18. M.F. Juárez, G. Soldano, H. Guesmi, F. Tielens, E. Santos, *Surf. Sci.*, 631 (2015) 235–247.
19. Y. Zhou, D. Wang, Y. Li, *Chem. Commun.*, 50 (2014) 6141.
20. S.W. Kang, Y.W. Lee, M. Kim, J.W. Hong, S.W. Han, *Chem. - An Asian J.*, 6 (2011) 909–913.
21. D. Chen, C. Li, H. Liu, F. Ye, J. Yang, *Sci. Rep.*, 5 (2015) 1–9.
22. N.R. Jana, L. Gearheart, C.J. Murphy, *Langmuir*, 17 (2001) 6782–6786.
23. Y. Garsany, O.A. Baturina, K.E. Swider-Lyons, S.S. Kocha, *Anal. Chem.*, 82 (2010) 6321–6328.
24. J.P. Oliveira, A.R. Prado, W.J. Keijok, M.R.N. Ribeiro, M.J. Pontes, B. V. Nogueira, M.C.C. Guimarães, *Arab. J. Chem.*, 13 (2020) 216–226.
25. D.K. Smith, B.A. Korgel, *Langmuir*, 24 (2008) 644–649.
26. Y. Okuno, K. Nishioka, N. Nakashima, Y. Niidome, *Chem. Lett.*, 38 (2009) 60–61.
27. H. Zhang, M. Jin, Y. Xiong, B. Lim, Y. Xia, *Acc. Chem. Res.*, 46 (2013) 1783–1794.
28. B. Lim, H. Kobayashi, T. Yu, J. Wang, M.J. Kim, Z.-Y. Li, M. Rycenga, Y. Xia, *J. Am. Chem. Soc.*, 132 (2010) 2506–2507.
29. M.S. Bakshi, *Cryst. Growth Des.*, 16 (2016) 1104–1133.
30. S.K. Meena, S. Celiksoy, P. Schäfer, A. Henkel, C. Sönnichsen, M. Sulpizi, *Phys. Chem. Chem. Phys.*, 18 (2016) 13246–13254.
31. J. Sun, Y. Han, H. Fu, X. Qu, Z. Xu, S. Zheng, *Chem. Eng. J.*, 313 (2017) 1–9.
32. G. Ramos-Sánchez, H. Yee-Madeira, O. Solorza-Feria, *Int. J. Hydrogen Energy*, 33 (2008) 3596–3600.
33. D.C. Martínez-Casillas, G. Vázquez-Huerta, J.F. Pérez-Robles, O. Solorza-Feria, *J. Power Sources*, 196 (2011) 4468–4474.
34. Q. Shi, H. Liang, D. Feng, J. Wang, G.D. Stucky, *J. Am. Chem. Soc.*, 130 (2008) 5034–5035.
35. L. Wang, Y. Yamauchi, *J. Am. Chem. Soc.*, 132 (2010) 13636–13638.
36. T. Vidaković, M. Christov, K. Sundmacher, *Electrochim. Acta*, 52 (2007) 5606–5613.
37. B. Ruiz Camacho, M. Torres Rodríguez, O. Solorza-Feria, *J. New Mater. Electrochem. Syst.*, 12 (2009) 43–47.
38. Q. Tan, C. Du, G. Yin, P. Zuo, X. Cheng, M. Chen, *J. Catal.*, 295 (2012) 217–222.